ISSN 1674-1056
http://cpb.iphy.ac.cn
http://iopscience.iop.org/cpb
中国物理 B
Chinese Physics
中国物理
Chinese Physics B

Harvesting base vibration energy by a piezoelectric inverted beam with pendulum

Jia-Nan Pan(潘家楠), Wei-Yang Qin(秦卫阳), Wang-Zheng Deng(邓王蒸), Hong-Lei Zhou(周红磊)

Citation: Chin. Phys. B . 2019, 28(1): 017701. **doi:** 10.1088/1674-1056/28/1/017701

Journal homepage: http://cpb.iphy.ac.cn; http://iopscience.iop.org/cpb

What follows is a list of articles you may be interested in

Transport of velocity alignment particles in random obstacles

Wei-jing Zhu(朱薇静), Xiao-qun Huang(黄小群), Bao-quan Ai(艾保全)

Chin. Phys. B . 2018, 27(8): 080504. **doi:** 10.1088/1674-1056/27/8/080504

Stochastic resonance in an under-damped bistable system driven by harmonic mixing signal

Yan-Fei Jin(靳艳飞)

Chin. Phys. B . 2018, 27(5): 050501. **doi:** 10.1088/1674-1056/27/5/050501

Stoney formula for piezoelectric film/elastic substrate system

Wang-Min Zhou(周旺民), Wang-Jun Li(李望君), Sheng-Yun Hong(洪圣运), Jie Jin(金杰), Shu-Yuan Yin(尹姝媛)

Chin. Phys. B . 2017, 26(3): 037701. **doi:** 10.1088/1674-1056/26/3/037701

Prompt efficiency of energy harvesting by magnetic coupling of an improved bi-stable system

Hai-Tao Li(李海涛), Wei-Yang Qin(秦卫阳)

Chin. Phys. B . 2016, 25(11): 110503. **doi:** 10.1088/1674-1056/25/11/110503

Collective dynamics in a non-dissipative two-coupled pendulum system

Chen Zi-Chen, Li Bo, Qiu Hai-Bo, Xi Xiao-Qiang

Chin. Phys. B . 2014, 23(5): 050506. **doi:** 10.1088/1674-1056/23/5/050506

Harvesting base vibration energy by a piezoelectric inverted beam with pendulum*

Jia-Nan Pan(潘家楠), Wei-Yang Qin(秦卫阳)†, Wang-Zheng Deng(邓王蒸), and Hong-Lei Zhou(周红磊)

Department of Engineering Mechanics, Northwestern Polytechnical University, Xi'an 710072, *China*

(Received 16 August 2018; revised manuscript received 4 October 2018; published online 30 December 2018)

We proposed a two-degrees-of-freedom inverted piezoelectric beam with pendulum to promote the performance of vibration energy harvesting. This configuration is composed of an inverted elastic beam and a pendulum attached to its free end. The electromechanical equations governing the nonlinear system were derived. The harmonic balance method (HBM) is applied to solve the equation and the results prove that there exists a 1:3 super-harmonic resonance. The simulation results show that owing to the particular nonlinearity, there appears a special bending effect in the amplitude-frequency response, i.e., bending right for the first natural frequency and left for the second natural frequency, which is beneficial for harvesting vibration energy. The HBM results are verified by the entity simulations. Furthermore, over a relatively wide range of power spectral density, it could reach a dense jumping and give a dense high pulse voltage.

Keywords: stochastic excitation, energy harvesting, inverted piezoelectric beam, pendulum, bi-stable state

PACS: 77.65.–j, 05.40.–a **DOI:** 10.1088/1674-1056/28/1/017701

1. Introduction

Vibration-based energy harvesting has been well studied as a promising approach to convert ambient kinetic energy into electrical energy in recent years.[1] These energy harvesting technologies provide an alternative way to powerful small-scale, low-power-consumption electronic devices and self-powered networks. Conventional energy harvesters are mostly based on linear oscillation, which are highly efficient when the excitation frequency is in the proximity of the resonance frequency. Namely, linear energy harvesters are only suitable for stationary and narrow band excitations. Whereas various kinds of nonlinear harvesters have been proved to be beneficial for solving the bandwidth limitation problem of linear harvesters. In light of this, an approach based on the exploitation of nonlinear oscillation has been proposed to overcome these drawbacks.[2–9]

In a nonlinear dynamical system, there exist some particular phenomena, e.g., super-harmonic resonance, sub-harmonic resonance, or internal resonance. They take place in the case that a natural frequency of the system approaches an integer ratio to that of another natural frequency. In the cases of resonance, it is possible to realize energy transfer between different modes. This characteristic was utilized as an invaluable method for the enhancement of energy harvesting. Chen *et al.* proposed an internal resonance energy harvester with snap-through nonlinearity which can produce more power.[10–12] Yang *et al.* proposed a harvester consisting of two cantilevers with a permanent magnet on their tips. This design shows an internal resonance mechanism that can broaden the frequency bandwidth.[13] Xu *et al.* studied a multi-directional energy harvester consisting of a piezoelectric cantilever with a pendulum attached to the tip. The modal energy interchange between beam vibration and pendulum motion can be induced due to internal resonance.[14,15] Xiong *et al.* exploited an internal resonance-based energy harvesting device which is composed of a primary oscillator with a tuned auxiliary oscillator. Various analysis methods indicate the enhancement of energy harvesting.[16,17] Wu *et al.* demonstrated a two-degrees-of-freedom energy harvester based on 1:3 internal resonance to realize the frequency up-converting effect.[18] These systems based on the 1:2 or 1:3 internal resonance mechanism greatly improve energy harvesting.

Different from the nonlinear energy harvesting devices using nonlinear resonance mechanism, the bi-stable[19,20] and multi-stable harvesters have been developed, which are usually made of beams, moveable and fixed magnets.[21] The inter-well motion of multi-stable system can lead to a large-amplitude oscillation and enhance the energy harvesting efficiency. Erturk *et al.* proposed a broadband bi-stable piezomagnetoelastic energy harvester and the numerical and experimental results demonstrated that the output voltage and output power of this bi-stable system were improved dramatically.[22] Zhou *et al.* demonstrated a magnetically coupled nonlinear energy harvester with rotatable magnets which can broaden the broadband of the harvester.[23] Li *et al.* investigated a tri-stable energy harvesting system, and the response under random excitation indicated that the tri-stable system can create high output voltage at the low intensity of stochastic excitation.[24] Zhou *et al.* studied a series of asymmetric tri-stable energy harvesters, where the asymmetric characteristic of the system

*Project supported by the National Natural Science Foundation of China (Grant No. 11672237) .

†Corresponding author. E-mail: qinweiyang@aliyun.com

© 2019 Chinese Physical Society and IOP Publishing Ltd

can be beneficial for the energy harvesting under various excitation conditions.[25] Lan *et al.* proposed an improved BEH by adding a magnet to reduce the barrier, and the system can realize a high output voltage even at weak excitation.[26]

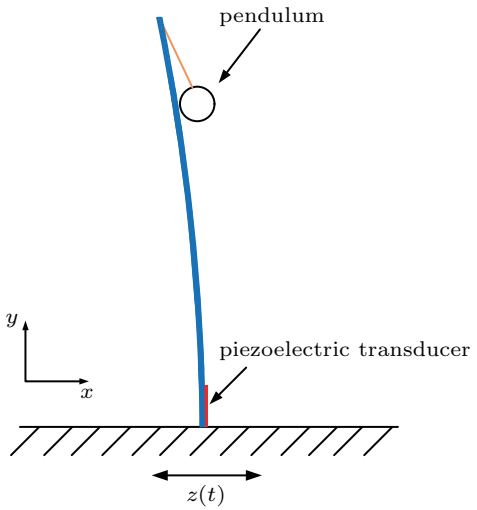


Fig. 1. Schematic of the inverted piezoelectric beam with pendulum (IPBP).

Nonlinear resonance mechanism and multi-stable motion are two primary ways for harvesters to enhance the ability of energy harvesting. Conventional nonlinear harvesters usually utilize one of them to realize high output. A few studies combined the two mechanisms in the existing literature. In this paper, we present a harvester consisting of an inverted beam with a pendulum. This combination is intended to use the interactive influence between them and the bi-stability to realize high amplitude vibration and output voltage. Considering that the inverted beam could turn to a bi-stable one in buckling state, some researchers focus on its application in scavenging vibration energy. The theoretical analysis and experimental validation of the inverted beam with a tip mass have been reported by several research groups.[27–29] The results indicate that the characteristics of inverted beam can benefit the energy harvesting significantly. To further enhance the harvesting ability, we propose an inverted beam with pendulum. The combination of an inverted beam and a pendulum transfers the original 1-DOF system into 2-DOF system. Hence, this paper proposed an energy harvester based on the exploitation of the properties of internal resonance and bi-stable characteristic. The configuration of the device is shown in Fig. 1. The energy harvester system is composed of an inverted beam with a pendulum connected to the free end. A piezoelectric transducer is bonded near the root of cantilever beam. The rest of the article is organized as follows. In Section 2, the governing equations are presented based on Lagrange's equations. In Section 3, frequency responses obtained in Simulink and COMSOL are discussed. In Section 4, the harmonic balance method is used to reveal the modal interaction. In Section 5 we investigate the motion under random excitation in unstable situations. Section 6 ends with conclusions.

2. Governing electromechanical equation

In this section, the governing electromechanical equation will be derived based on the Euler–Bernoulli beam theory and Lagrange equation. First, some preliminary assumptions need to be made. The thickness of the beam is smaller than its length, so the effects of shear deformation and rotary inertia of the beam are neglected. A shape function is utilized to approximate the inverted beam's deflection. The string of the pendulum is assumed to be massless and inextensible. The longitudinal deformation of the inverted beam is neglected. The system is excited by base motion in the X direction.

Since the proposed device comprises an inverted beam and a pendulum, it can be simplified as a 2-DOF system. The kinetic and potential energies of the system are

$$\begin{aligned} T &= \frac{1}{2}\rho_{\mathrm{b}}A_{\mathrm{b}}\int_0^{l_{\mathrm{b}}}[\dot{w}(y,t)+\dot{z}x]^2\,\mathrm{d}y \\ &\quad+\frac{1}{2}\rho_{\mathrm{p}}A_{\mathrm{p}}\int_0^{l_{\mathrm{p}}}[\dot{w}(y,t)+\dot{z}x]^2\,\mathrm{d}y \\ &\quad+\frac{1}{2}m[\dot{w}(l_{\mathrm{b}},t)+\dot{\varphi}l\cos\varphi+\dot{z}x]^2+\frac{1}{2}m(\dot{\varphi}l\sin\varphi)^2, \quad (1) \\ U &= \frac{1}{2}\int_0^{l_{\mathrm{b}}}E_{\mathrm{b}}I_{\mathrm{b}}(w''(y,t))^2\,\mathrm{d}y \\ &\quad+\frac{1}{2}\int_0^{l_{\mathrm{p}}}E_{\mathrm{p}}I_{\mathrm{p}}(w''(y,t))^2\,\mathrm{d}y+mgl(1-\cos\varphi) \\ &\quad-\int_0^{l_{\mathrm{b}}}\gamma_{\mathrm{c}}vw''(y,t)\,\mathrm{d}y+\frac{1}{2}C_{\mathrm{p}}v^2. \quad (2) \end{aligned}$$

The work done by the nonconservative forces can be given by

$$\delta W=-c_1\int_0^{l_{\mathrm{b}}}\dot{w}(y,t)\delta w(y,t)\,\mathrm{d}y-c_2\dot{\varphi}\delta\varphi+Q(t)\delta v. \quad (3)$$

The coordinate $w(yt)$ represents the transverse displacement at any point in the inverted beam, while the coordinate φ represents the angular displacement of the pendulum with respect to the y-axis. m is the mass of the pendulum, g is the gravitational acceleration, z_x is the base motion, l is the length of the string, c_1 and c_2 are the corresponding viscous damping coefficients, respectively, C_{p} is the capacitance of the piezoelectric transducer, γ_{c} is the electromechanical coupling term, $v(t)$ represents the voltage across the piezoelectric layer, and $Q(t)$ is the electric charge of the piezoelectric layer. Let ρ_{b}, A_{b}, l_{b}, E_{b}, and I_{b} represent the mass density of the beam, the cross-sectional area of the beam, the length of the inverted beam, Young's modulus of the beam, the moment of inertia of the beam; and those of the piezoelectric transducer are denoted by subscript p. The beam's transverse displacement $w(yt)$ can be approximated by a shape function $\Psi(y)$ and the tip displacement $q(t)$,

$$w(y,t)=\psi(y)q(t), \quad (4)$$

where the shape function $\psi(y)$ is of the form

$$\psi(y) = 1 - \cos\left(\frac{\pi y}{2l_b}\right). \tag{5}$$

The Lagrange equation is applied to obtain the equations of motion of the system,

$$\begin{aligned}
&\frac{\mathrm{d}}{\mathrm{d}t}\left(\frac{\partial L}{\partial \dot{q}}\right) - \frac{\partial L}{\partial q} = \frac{\delta W}{\partial q},\\
&\frac{\mathrm{d}}{\mathrm{d}t}\left(\frac{\partial L}{\partial \dot{\varphi}}\right) - \frac{\partial L}{\partial \varphi} = \frac{\delta W}{\partial \varphi},\\
&\frac{\mathrm{d}}{\mathrm{d}t}\left(\frac{\partial L}{\partial \dot{v}}\right) - \frac{\partial L}{\partial v} = \frac{\delta W}{\partial v},
\end{aligned} \tag{6}$$

where $L = T - U$; then the governing equation of the IPBP subjected to base excitation $\ddot{z}_x$ can be derived as

$$\begin{aligned}
&(M+m)\ddot{q} + c_1\dot{q} + Kq + ml(\ddot{\varphi} - \dot{\varphi}^2\varphi) + \chi v\\
&= -(M_1+m)\ddot{z}x,\\
&ml^2\ddot{\varphi} + c_2\dot{\varphi} + ml\ddot{q} + mgl\varphi = -ml\ddot{z}x,\\
&\frac{v}{R} - \chi\dot{q} + C_p\dot{v} = 0,
\end{aligned} \tag{7}$$

where M is the mass of the inverted piezoelectric beam, M_1 is the modal mass, K is the mechanical stiffness of the inverted piezoelectric beam, R is the resistance load, χ is the electromechanical coupling of the transducer,

$$\begin{aligned}
M &= \rho_b A_b \int_0^{l_b} \psi^2\,\mathrm{d}y + \rho_p A_p \int_0^{l_p} \psi^2\,\mathrm{d}y,\\
M_1 &= \rho_b A_b \int_0^{l_b} \psi\,\mathrm{d}y + \rho_p A_p \int_0^{l_p} \psi\,\mathrm{d}y,\\
K &= \int_0^{l_b} E_b I_b (\psi'')^2\,\mathrm{d}y + \int_0^{l_p} E_p I_p (\psi'')^2\,\mathrm{d}y,\\
\chi &= \int_0^{l_p} \gamma_c \psi''\,\mathrm{d}y.
\end{aligned} \tag{8}$$

The proposed piezoelectric structure is different from the general kinetic model because of the inertia coupling, namely, there are coupling terms in the quality matric. Then the two natural frequencies of the 2DOF systems are

$$\begin{aligned}
&\omega_{1,2}^2 = \frac{\hat{\omega}_1^2 + \hat{\omega}_2^2 \pm \sqrt{(\hat{\omega}_2^2 - \hat{\omega}_1^2)^2 + 4r_m\hat{\omega}_1^2\hat{\omega}_2^2}}{2(1-r_m)},\\
&\hat{\omega}_1^2 = \frac{g}{l};\quad \hat{\omega}_2^2 = \frac{K}{M+m};\quad r_m = \frac{m}{M+m},\quad r_m \in (0,1).
\end{aligned} \tag{9}$$

It should be noted that there exists a nonlinear term $\dot{\varphi}^2\varphi$ in the equation, which may give rise to super-harmonic resonance and energy transfer between modes. For validation, we adjust the mechanical parameters of the piezoelectric system so that the necessary condition for 1:3 super-harmonic resonance is met. Finally, by precisely adjusting parameters, the natural frequencies of the 2-DOF system could be designed as

$$f_1 = 2.2\ \text{Hz},$$

$$f_2 = 6.6\ \text{Hz}. \tag{10}$$

This design is utilized in the following simulation to verify the theoretical results of 1:3 super-harmonic resonance.

By introducing some parameters, the governing equation (Eq. (7)) can be simplified into the following dimensionless form:

$$\begin{aligned}
&\ddot{u} + r_m\ddot{\varphi} - r_m\dot{\varphi}^2\varphi + c_1'\dot{u} + \hat{\omega}_1^2 u + \chi' V = -\gamma\frac{\ddot{z}_x}{l},\\
&\ddot{\varphi} + \ddot{u} + c_2'\dot{\varphi} + \hat{\omega}_2^2\varphi = -\frac{\ddot{z}_x}{l},\\
&\frac{V}{R} - \chi\dot{u} + C_p\dot{V} = 0,
\end{aligned} \tag{11}$$

where $u = \frac{q}{l}$, $V = \frac{v}{l}$, $c_1' = \frac{c_1}{(M+m)l}$, $c_2' = \frac{c_2}{ml}$, $\chi' = \frac{\chi}{M+m}$, and $\gamma = \frac{M_1+m}{M+m}$. The governing equation can be simplified by the parameters defined above.

3. Frequency responses

For validation, an entity model is established in the COMSOL, and the corresponding simulation is carried out. First, the entity model is excited by the harmonic motion with sweeping frequency. Hence, the amplitude-frequency responses are acquired. Because the nonlinear system exhibits different characteristics for different frequency sweeping directions, both forward sweeping and backward sweeping were performed in simulations. As for the harvesting circuit, the open-circuit condition was adopted. Moreover, the parameters utilized in the study are listed in Table 1.

As for the entity model, it is established by the multi-physical field software COMSOL. The involved physical components are multi-body dynamical, piezoelectric, and electric, respectively. The finite element model of the IPBP includes an inverted beam with a piezoelectric patch and a pendulum. The inverted beam is an elastic one and the pendulum is a lumped mass connected to beam's top with a string. The inverted beam is clamped to the base. The base is assumed to oscillate horizontally (X axis direction).

Table 1. Parameter values used in the Simulink and Comsol.

Parameter	Values
Inverted beam size/mm^3	190×8× 0.6
PZT size/mm^3	30×8× 0.3
Length of the pendulum, l/mm	27.5
Mass density of the beam, ρ_b/kg·m^{-3}	7850
Mass density of the PZT, ρ_p/kg·m^{-3}	7500
Young's modulus of the beam, E_b/GPa	109
Young's modulus of the PZT, E_p/GPa	106
Coupling coefficient, χ/N·V^{-1}	0.00001
Resistance, R/kΩ	10000
Capacitance, C_p/nF	20

Table 2. Element type and element number.

Element type	Element number
Triangular elements	86
Quadrilateral elements	375
Edge elements	245
Vertex elements	10

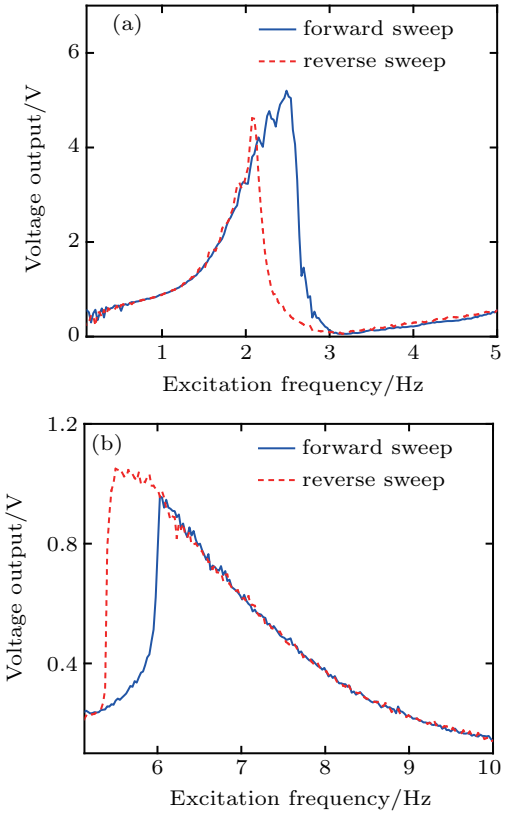


Fig. 2. Output voltage obtained in COMSOL: (a) first primary resonance, (b) second primary resonance.

The simulation in COMSOL used four elements: the triangular element, the quadrilateral element, the edge element, and the vertex element. The number of each element is shown in Table 2. The fixed constraint is applied to the bottom boundary of the inverted beam, thus the displacements of nodes at bottom boundary in the x and y direction are both 0. The simulation for the entity model was carried out, and the results are shown in Figs. 2 and 3. The voltage amplitude–frequency responses are illustrated in Fig. 2. For clarity, the curve is separated into two figures, Figs. 2(a) and 2(b). Duffing nonlinearity[30–33] can be found in the responses. From Fig. 2(a), it can be seen that the amplitude–frequency response near the first natural frequency shows obvious harden-spring feature, i.e., bending right; in Fig. 2(b), the response near the second natural frequency shows the soften-spring feature, i.e., bending left. Different bending direction of amplitude–frequency responses tends to form a region of multiple solutions over the frequency range between the first and second natural frequencies. This is beneficial for harvesting vibration energy. Multiple solutions and jumping phenomenon induced by the nonlinear term could realize a broadband high output. In contrast, if at the tip the beam has a mass rather than a pendulum, the nonlinear effect will be weak. This design was tried in COMSOL as well and the amplitude–frequency response was obtained, as shown in Fig. 3. It is apparent that the sweeping direction has a slight influence on the amplitude–frequency response, which suggests that the proposed IPBP could increase the frequency bandwidth considerably. The existence of harden- and soften-spring features in the first and second natural frequencies introduces multiple solution areas between the two primary resonance frequencies. In practice, the proposed energy harvester could generate a high output voltage.

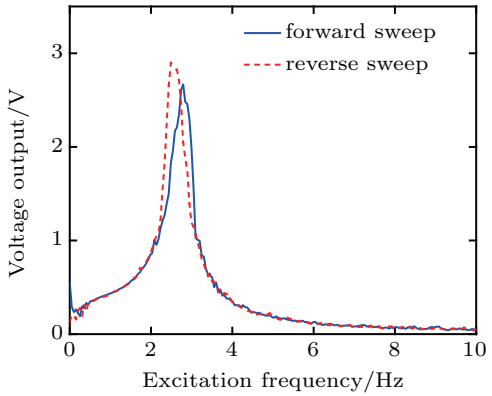


Fig. 3. Amplitude–frequency response of tip-mass design.

4. Time responses

4.1. HBM solutions and numerical simulation

In this subsection, the harmonic balance method (HBM) is introduced to solve the electromechanical equation (Eq. (11)). According to the HBM, the solution of nonlinear/linear system should be in the form of truncated Fourier series, i.e.,

$$x(t) = \sum_{n=1}^{N} [A_n \cos(n\Omega t) + B_n \cos(n\Omega t)], \tag{12}$$

where A_n and B_n are defined as the solution's Fourier coefficients, and the subscript n is the order of harmonic components.

Considering that the nonlinear term $\dot{\varphi}^2\varphi$ may lead to 1:3 super-harmonic resonance, without loss of generality, the solution is assumed to own the corresponding harmonic components, i.e., Ω, 2Ω, and 3Ω, when the system is excited by an external harmonic excitation of angular frequency. Thus, the solutions take the following forms:

$$\begin{aligned} u &= A_{11}\cos\Omega t + B_{11}\sin\Omega t + A_{12}\cos 2\Omega t \\ &\quad + B_{12}\sin 2\Omega t + A_{13}\cos 3\Omega t + B_{13}\sin 3\Omega t, \\ \varphi &= A_{21}\cos\Omega t + B_{21}\sin\Omega t + A_{22}\cos 2\Omega t \\ &\quad + B_{22}\sin 2\Omega t + A_{23}\cos 3\Omega t + B_{23}\sin 3\Omega t, \end{aligned}$$

$$\begin{aligned} V &= A_{31}\cos\Omega t + B_{31}\sin\Omega t + A_{32}\cos 2\Omega t \\ &\quad + B_{32}\sin 2\Omega t + A_{33}\cos 3\Omega t + B_{33}\sin 3\Omega t. \end{aligned} \tag{13}$$

Then their first derivatives with respect to time t are

$$\begin{aligned} \dot{u} &= -A_{11}\Omega\sin\Omega t + B_{11}\Omega\cos\Omega t \\ &\quad - 2A_{12}\Omega\sin 2\Omega t + 2B_{12}\Omega\cos 2\Omega t \\ &\quad - 3A_{13}\Omega\sin 3\Omega t + 3B_{13}\Omega\cos 3\Omega t, \\ \dot{\varphi} &= -A_{21}\Omega\sin\Omega t + B_{21}\Omega\cos\Omega t \\ &\quad - 2A_{22}\Omega\sin 2\Omega t + 2B_{22}\Omega\cos 2\Omega t \\ &\quad - 3A_{23}\Omega\sin 3\Omega t + 3B_{23}\Omega\cos 3\Omega t, \\ \dot{V} &= -A_{31}\Omega\sin\Omega t + B_{31}\Omega\cos\Omega t \\ &\quad - 2A_{32}\Omega\sin 2\Omega t + 2B_{32}\Omega\cos 2\Omega t \\ &\quad - 3A_{33}\Omega\sin 3\Omega t + 3B_{33}\Omega\cos 3\Omega t. \end{aligned} \tag{14}$$

Furthermore, the second derivatives of u and φ are

$$\begin{aligned} \ddot{u} &= -A_{11}\Omega^2\cos\Omega t - B_{11}\Omega^2\sin\Omega t \\ &\quad - 4A_{12}\Omega^2\cos 2\Omega t - 4B_{12}\Omega^2\sin 2\Omega t \\ &\quad - 9A_{13}\Omega^2\cos 3\Omega t - 9B_{13}\Omega^2\sin 3\Omega t, \\ \ddot{\varphi} &= -A_{21}\Omega^2\cos\Omega t - B_{21}\Omega^2\sin\Omega t \\ &\quad - 4A_{22}\Omega^2\cos 2\Omega t - 4B_{22}\Omega^2\sin 2\Omega t \\ &\quad - 9A_{23}\Omega^2\cos 3\Omega t - 9B_{23}\Omega^2\sin 3\Omega t. \end{aligned} \tag{15}$$

On the other hand, the nonlinear term $\dot{\varphi}^2\varphi$ in the governing equation can be expanded into Fourier series, i.e.,

$$\dot{\varphi}^2\varphi = \sum_{n=1}^{3}\left[\bar{A}n\cos(n\Omega t) + \bar{B}_n\sin(n\Omega t)\right], \tag{16}$$

where the coefficients of each harmonic component can be given by

$$\begin{aligned} \bar{A}_n &= \frac{\Omega}{2\pi}\int_0^{2\pi/\Omega} s_2^2 s_1\cos(n\Omega t)\,\mathrm{d}t, \\ \bar{B}_n &= \frac{\Omega}{2\pi}\int_0^{2\pi/\Omega} s_2^2 s_1\sin(n\Omega t)\,\mathrm{d}t, \\ s_1 &= A_{21}\cos\Omega t + B_{21}\sin\Omega t + A_{22}\cos 2\Omega t \\ &\quad + B_{22}\sin 2\Omega t + A_{23}\cos 3\Omega t + B_{23}\sin 3\Omega t, \\ s_2 &= -A_{21}\Omega\sin\Omega t + B_{21}\Omega\cos\Omega t - 2A_{22}\Omega\sin 2\Omega t \\ &\quad + 2B_{22}\Omega\cos 2\Omega t - 3A_{23}\Omega\sin 3\Omega t \\ &\quad + 3B_{23}\Omega\cos 3\Omega t. \end{aligned} \tag{17}$$

$$\begin{aligned} &(-A_{11}\Omega^2\cos\Omega t - B_{11}\Omega^2\sin\Omega t \\ &-4A_{12}\Omega^2\cos 2\Omega t - 4B_{12}\Omega^2\sin 2\Omega, \\ &-9A_{13}\Omega^2\cos 3\Omega t - 9B_{13}\Omega^2\sin 3\Omega t) \\ &+r_m(-A_{21}\Omega^2\cos\Omega t - B_{21}\Omega^2\sin\Omega t - 4A_{22}\Omega^2\cos 2\Omega t, \\ &-4B_{22}\Omega^2\sin 2\Omega t - 9A_{23}\Omega^2\cos 3\Omega t - 9B_{23}\Omega^2\sin 3\Omega t) \\ &-r_m\sum_{n=1}^{3}\left[\bar{A}n\cos(n\Omega t) + \bar{B}_n\sin(n\Omega t)\right], \\ &+c_1'(-A_{11}\Omega\sin\Omega t + B_{11}\Omega\cos\Omega t - 2A_{12}\Omega\sin 2\Omega t \\ &+2B_{12}\Omega\cos 2\Omega t - 3A_{13}\Omega\sin 3\Omega t + 3B_{13}\Omega\cos 3\Omega t), \\ &+\hat{\omega}_1^2(A_{11}\cos\Omega t + B_{11}\sin\Omega t + A_{12}\cos 2\Omega t \\ &+B_{12}\sin 2\Omega t + A_{13}\cos 3\Omega t + B_{13}\sin 3\Omega t), \\ &+\chi'(A_{31}\cos\Omega t + B_{31}\sin\Omega t + A_{32}\cos 2\Omega t \\ &+B_{32}\sin 2\Omega t + A_{33}\cos 3\Omega t + B_{33}\sin 3\Omega t) \\ &= -a_z\gamma\cos\Omega t/l, \end{aligned} \tag{19}$$

$$\begin{aligned} &(-A_{11}\Omega^2\cos\Omega t - B_{11}\Omega^2\sin\Omega t - 4A_{12}\Omega^2\cos 2\Omega t \\ &-4B_{12}\Omega^2\sin 2\Omega t - 9A_{13}\Omega^2\cos 3\Omega t - 9B_{13}\Omega^2\sin 3\Omega t), \\ &+(-A_{21}\Omega^2\cos\Omega t - B_{21}\Omega^2\sin\Omega t - 4A_{22}\Omega^2\cos 2\Omega t \\ &-4B_{22}\Omega^2\sin 2\Omega t - 9A_{23}\Omega^2\cos 3\Omega t - 9B_{23}\Omega^2\sin 3\Omega t), \\ &+c_2'(-A_{21}\Omega\sin\Omega t + B_{21}\Omega\cos\Omega t - 2A_{22}\Omega\sin 2\Omega t \\ &+2B_{22}\Omega\cos 2\Omega t - 3A_{23}\Omega\sin 3\Omega t + 3B_{23}\Omega\cos 3\Omega t), \\ &+\hat{\omega}_2^2(A_{21}\cos\Omega t + B_{21}\sin\Omega t + A_{22}\cos 2\Omega t + B_{22}\sin 2\Omega t \\ &+A_{23}\cos 3\Omega t + B_{23}\sin 3\Omega t) = -a_z\cos\Omega t/l, \end{aligned} \tag{20}$$

$$\begin{aligned} &1/R(A_{31}\cos\Omega t + B_{31}\sin\Omega t + A_{32}\cos 2\Omega t \\ &+B_{32}\sin 2\Omega t + A_{33}\cos 3\Omega t + B_{33}\sin 3\Omega t), \\ &-\chi(-A_{11}\Omega\sin\Omega t + B_{11}\Omega\cos\Omega t \\ &-2A_{12}\Omega\sin 2\Omega t + 2B_{12}\Omega\cos 2\Omega t, \\ &-3A_{13}\Omega\sin 3\Omega t + 3B_{13}\Omega\cos 3\Omega t) \\ &+C_{\mathrm{p}}(-A_{31}\Omega\sin\Omega t + B_{31}\Omega\cos\Omega t - 2A_{32}\Omega\sin 2\Omega t, \\ &+2B_{32}\Omega\cos 2\Omega t - 3A_{33}\Omega\sin 3\Omega t \\ &+3B_{33}\Omega\cos 3\Omega t) = 0. \end{aligned} \tag{21}$$

Equating the coefficients associated with each order of harmonics, i.e., $\cos(n\Omega t)$ or $\sin(n\Omega t)$, will yield eighteen algebraic equations with eighteen unknown coefficients. Considering that the eighteen algebraic equations are difficult to solve, the Newton–Raphson method is introduced to obtain the corresponding solutions.

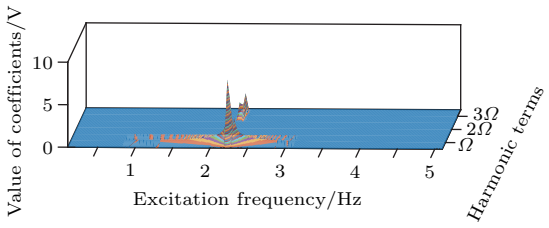


Fig. 4. Harmonic coefficients versus excitation frequency (corresponding to the output voltage V).

For an excitation with angular frequency Ω, the coefficients for the harmonic components can be solved from the eighteen algebraic equations in Appendix A. For each Ω, the corresponding coefficients of harmonics were solved and stored. Consequently, all stored results can be plotted as a

three-dimensional figure (Fig. 4). The excitation frequency ranges from 0.1 Hz to 5.1 Hz. As a result, from Fig. 4, it can be seen that the harmonic coefficient for Ω reaches the maximum value at the natural frequency of $f = 2.2$ Hz, while the 3Ω component appears and exhibits a peak; in contrast, the coefficient for 2Ω component is zero now. This result proves that for this configuration the nonlinear term of $\dot{\varphi}^2\varphi$ could induce a 1:3 super-harmonic resonance.

For clarity, the numerical simulations at some specific frequencies are carried out in Simulink. The sub-models in Simulink are assembled together to establish the whole dynamical model of IPBP. To show the spectrum feature of response, fast Fourier transform (FFT) is employed to estimate the spectrum components. The time-domain responses and frequency spectra under the excitations of 11 Hz and 2.2 Hz are illustrated in Figs. 5 and 6, respectively. It is evident that there exists an super-harmonic frequency component when the excitation frequency is at the first primary resonance (Fig. 6), whereas only the exciting frequency component exists when the system is excited non-resonantly (Fig. 5). It is worth noting that the response becomes modulated at resonance when the excitation level increases to $a_z = 0.02$ g (see Fig. 7).

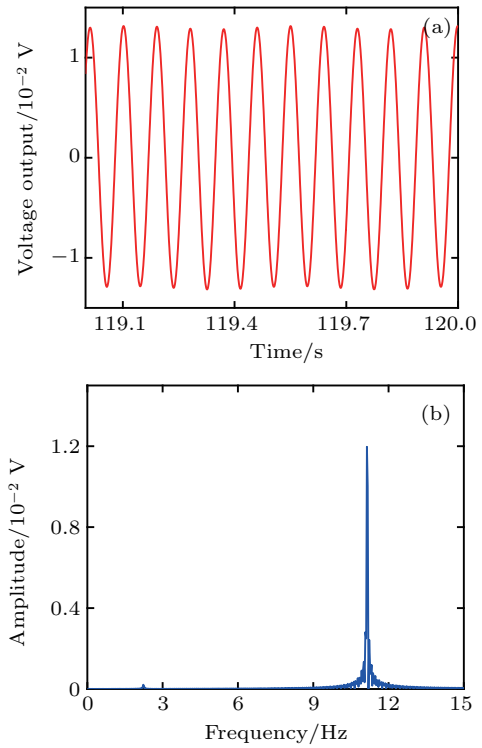


Fig. 5. (a) Non-resonant time history and (b) frequency spectrum of output voltage ($f = 11$ Hz, $a_z = 0.01$ g).

It should be noted that this system is composed of an inverted beam and a pendulum. It is interesting that at the two natural frequencies the beam and pendulum oscillate with different characteristics. When excited at the first natural frequency, the first primary resonance occurs and the first mode appears. As shown in Fig. 8, the beam and the pendulum oscillate synchronously, i.e., they have the same phase; when excited at the second natural frequency, the beam and the pendulum oscillate with opposite phases, i.e., they are anti-synchronous (see Fig. 9).

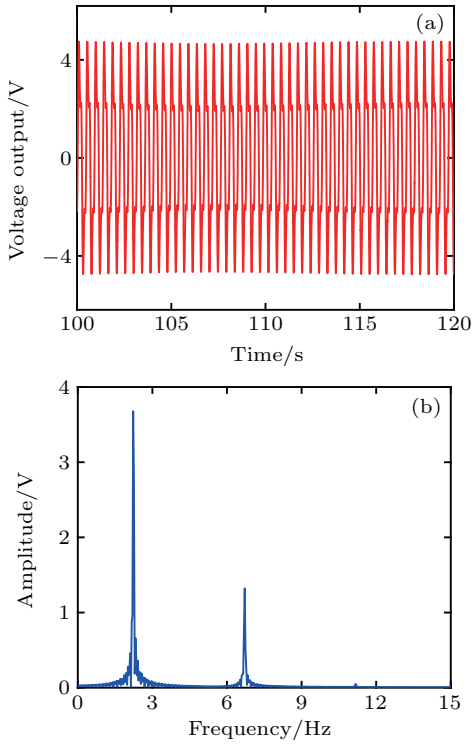


Fig. 6. (a) Resonant time history and (b) frequency spectrum of output voltage ($f = 2.2$ Hz, $a_z = 0.01$ g).

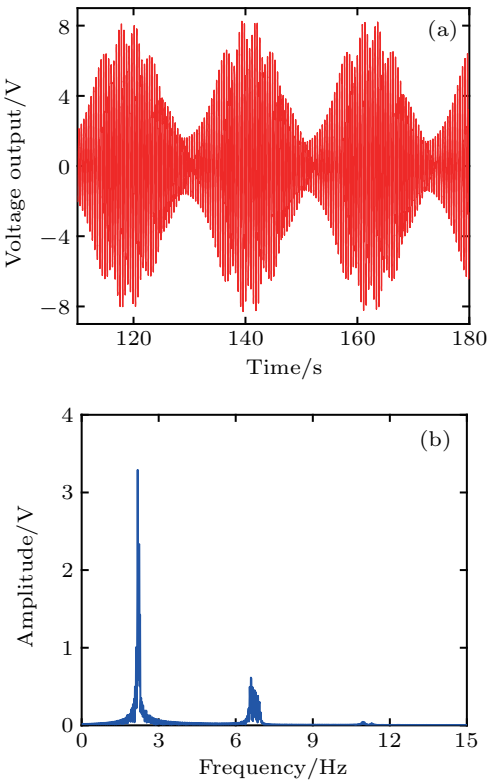


Fig. 7. (a) Resonant time history and (b) frequency spectrum of output voltage ($f = 2.2$ Hz, $a_z = 0.02$ g).

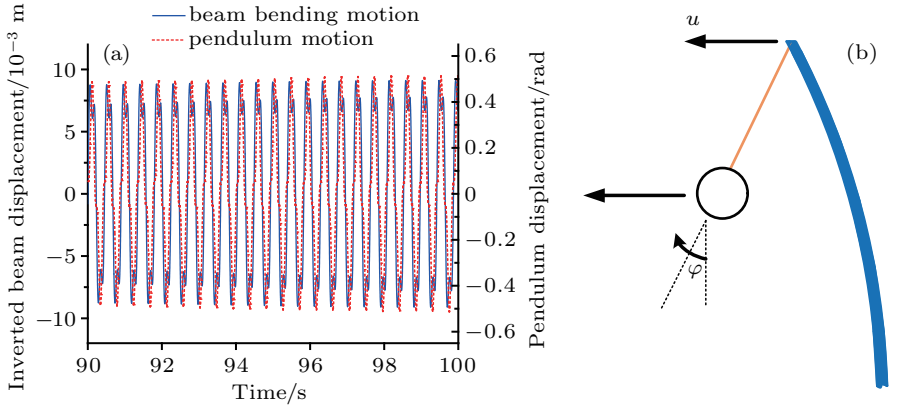


Fig. 8. The motion of the energy harvester at the first primary resonance: (a) time history of beam bending motion and pendulum motion; (b) pattern of the first mode.

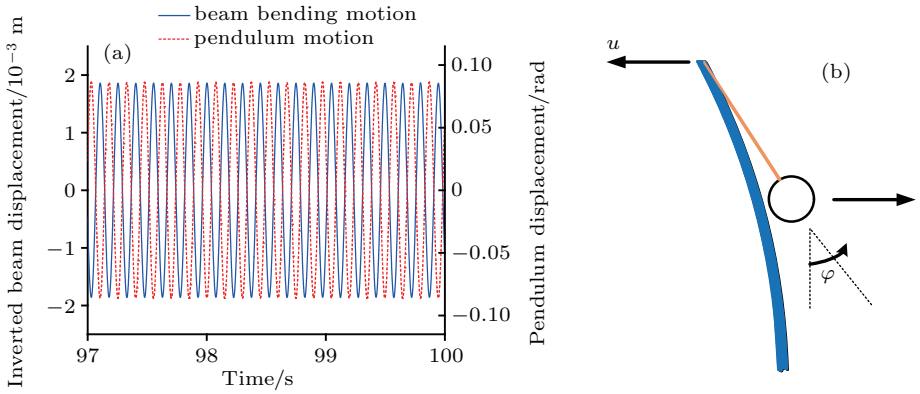


Fig. 9. The motion of the energy harvester at the second primary resonance: (a) time history of beam bending motion and pendulum motion; (b) pattern of the second mode.

4.2. Model and simulation in COMSOL

For validation, in the COMSOL the entity model was designed to be excited by the harmonic motions same as those in Section 4.1. The corresponding results are shown in Figs. 10–15. Figure 10 shows the response spectrum at $f = 11$ Hz. It is obvious that the exciting frequency is dominant. Then at $f = 2.2$ Hz, the response spectrum shows the appearance of a super-harmonic resonance; at $a_z = 0.02$ g, the response waveform suggests that there is a modulated phenomenon (see Fig. 11). This is in good agreement with the simulation by Simulink (see Fig. 7).

To show the modal characteristics, the entity model was excited by base motion at the two natural frequencies. When the excitation frequency is at the first natural frequency, the beam and pendulum will oscillate synchronously, i.e., their phases are the same, as shown in Fig. 12. This means that they will oscillate to the same direction at an instant. In contrast, when the excitation frequency is at the second natural frequency, the beam and pendulum will oscillate asynchronously, i.e., their phases are reverse, as shown in Fig. 13.

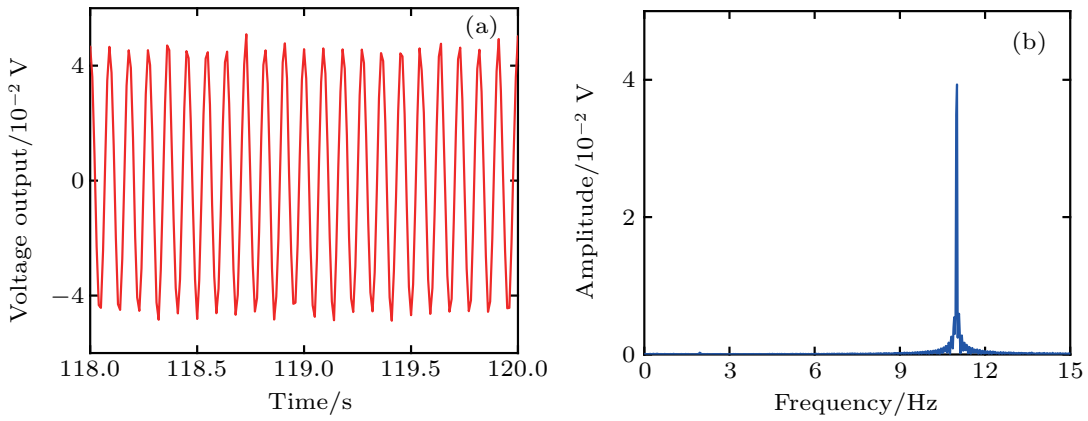


Fig. 10. (a) Non-resonant time history and (b) frequency spectrum of output voltage ($f = 11$ Hz, $a_z = 0.02$ g).

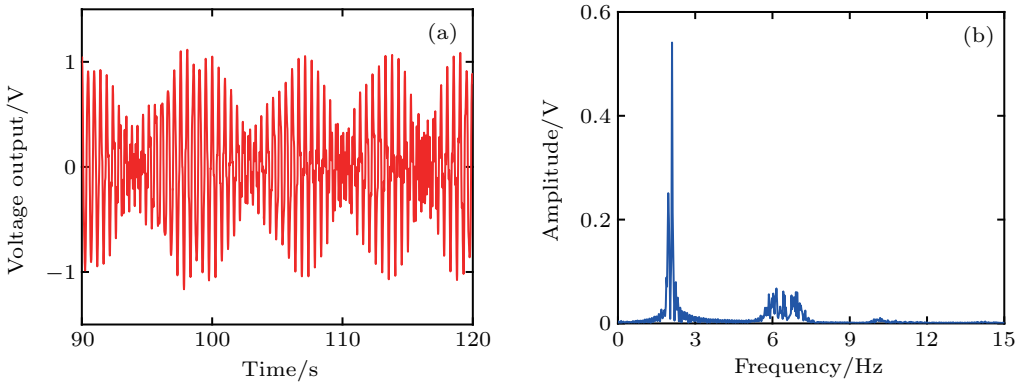


Fig. 11. Resonant time history and frequency spectrum of output voltage ($f = 2.2$Hz, $a_z = 0.02$ g).

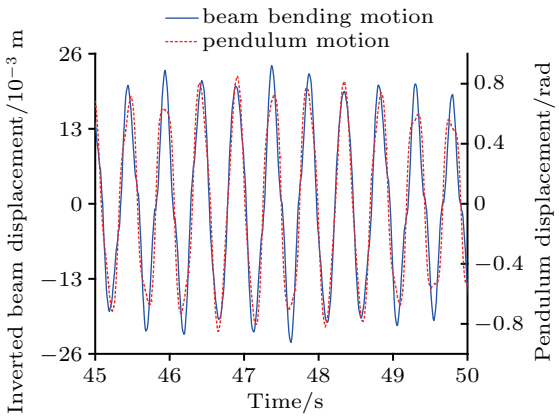


Fig. 12. Waveforms of the beam and pendulum motions at the first primary resonance.

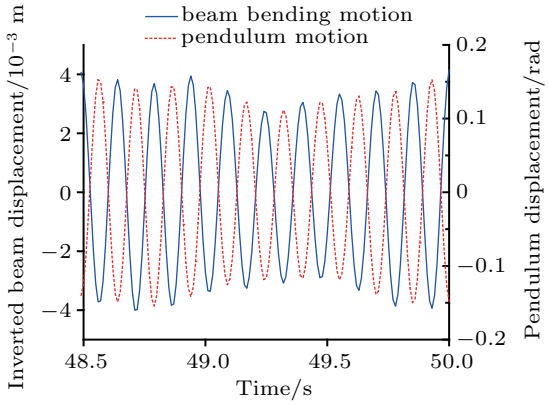


Fig. 13. Waveforms of the beam and pendulum motions at the second primary resonance.

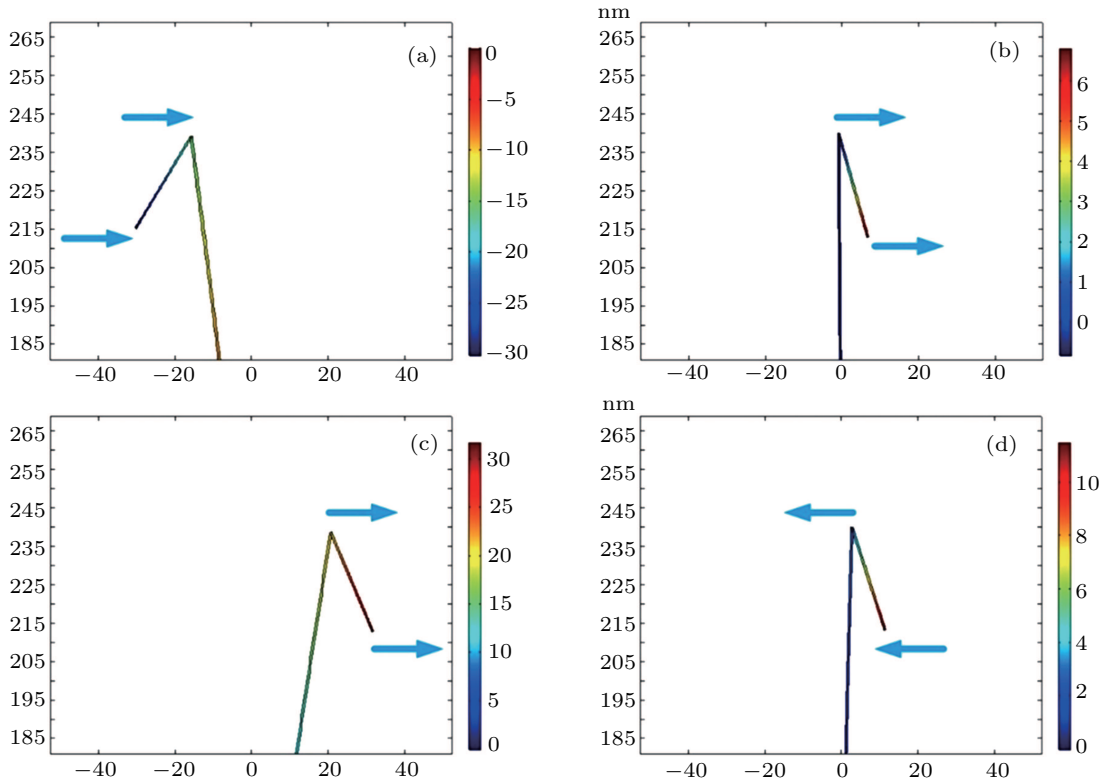


Fig. 14. Response patterns of the second mode at different times: (a) $t = 49.1$ s; (b) $t = 49.13$ s; (c) $t = 49.17$ s; (d) $t = 49.2$ s.

This means that they oscillate in the reverse direction at an instant. Then the response patterns at different instants of time are plotted in Figs. 14–16. The arrowhead indicates the motion of the tip and the pendulum, respectively. Figure 14 and 16(a) show

that the beam and pendulum oscillate toward the same direction when the excitation frequency is at the first natural frequency. In contrast, they oscillate in the reverse directions when the excitation frequency is at the second natural frequency, as shown in Figs. 15 and 16(b).

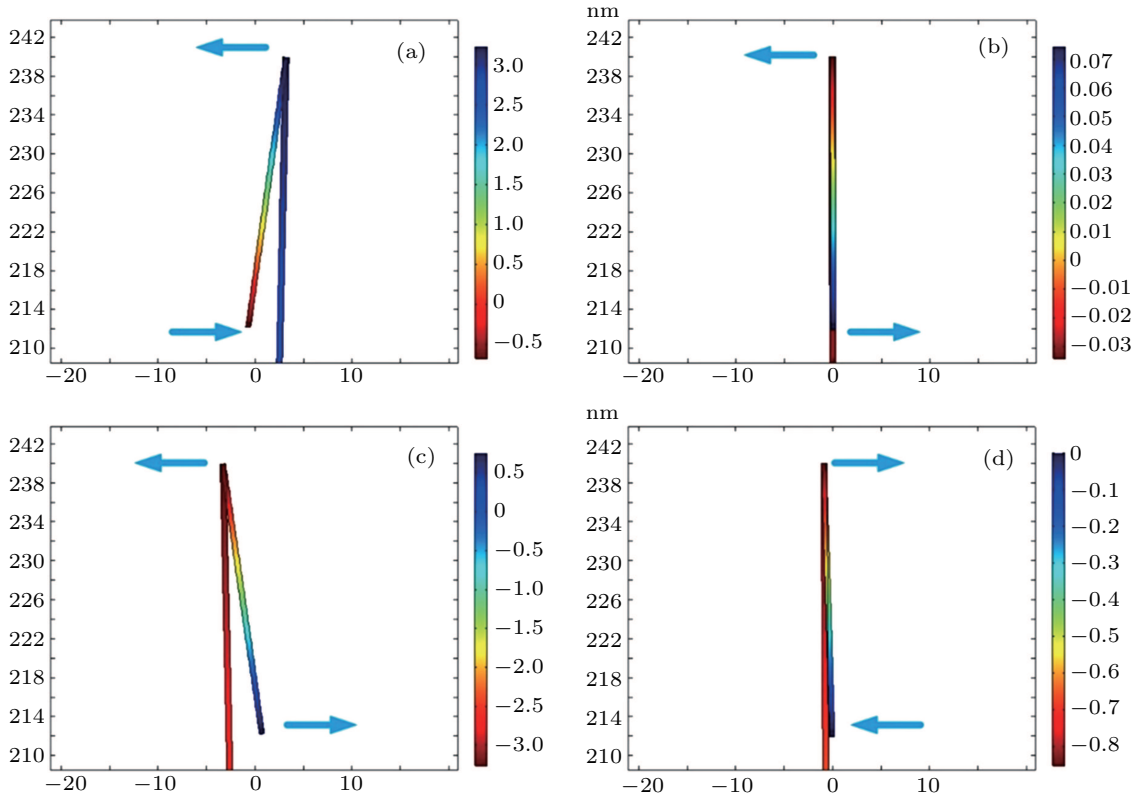


Fig. 15. Response patterns of the second mode at different times: (a) $t = 49.1$ s; (b) $t = 49.13$ s; (c) $t = 49.17$ s; (d) $t = 49.2$ s.

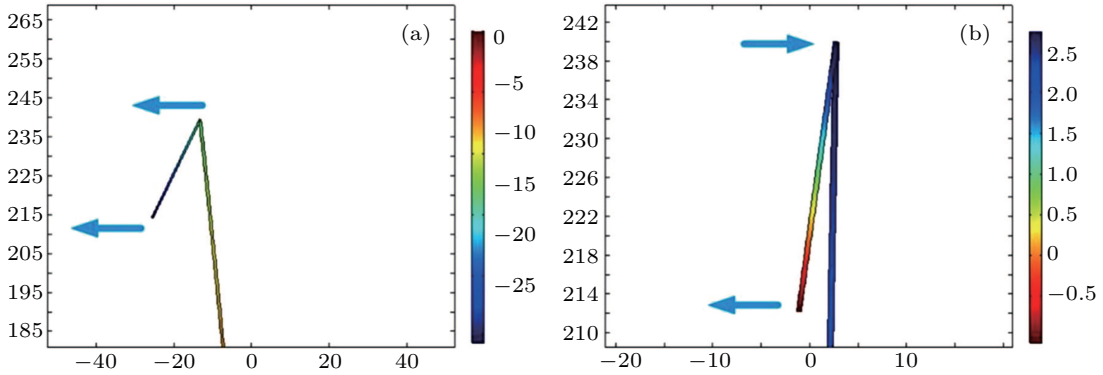


Fig. 16. Response patterns at different instants of time: (a) first mode at $t = 49.5$ s; (b) second mode at $t = 49.24$ s.

5. Entity model responses under stochastic excitation

To examine the performance of this configuration in harvesting energy, a band-limited white noise is introduced as the base excitation, which has a frequency range of 5–500 Hz and a varied excitation intensity (power spectrum density, PSD). The absence of the low-frequency component (< 5 Hz) in stochastic excitation aims to prove the effect of energy transfer between modes. In the following simulation, it can be found that the first mode oscillation could be excited by the band-limited noise without the first natural frequency (see Fig. 17). It should be noted that with the variation of pendulum mass the beam could be buckling or unbuckling, i.e., the beam could be the monostable or bi-stable one. The strain–time diagrams are obtained from the location near the root of the inverted beam, in which the piezoelectric patch is bonded. We studied both the two cases. In the unbuckling case, the weight of mass of the pendulum is 5 g, and the mass ratio is $r_{\mathrm{m}} = 0.64$; while in the buckling case, the weight of mass of the pendulum is 30 g, and the mass ratio is $r_{\mathrm{m}} = 0.91$.

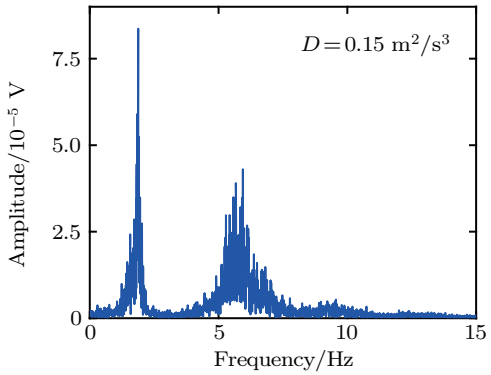


Fig. 17. Frequency spectrum of strain at excitation of PSD = 0.15 m^2/s^3.

5.1. Unbuckling case

Suppose that the mass is small ($m = 5$ g) and the beam is unbuckling. The stochastic base excitation is applied to the monostable system in the COMSOL, and the simulation is carried out for several intensities, which are varied at PSD = 0.15 m^2/s^3, 0.20 m^2/s^3, 0.25 m^2/s^3, and 0.30 m^2/s^3. The corresponding results were obtained, which are shown in Figs. 18–21. It is evident that in the unbuckling case the system generally oscillates around the trivial stable equilibrium point $x = 0$, thus the strain is relatively small, and the output voltage is fairly low.

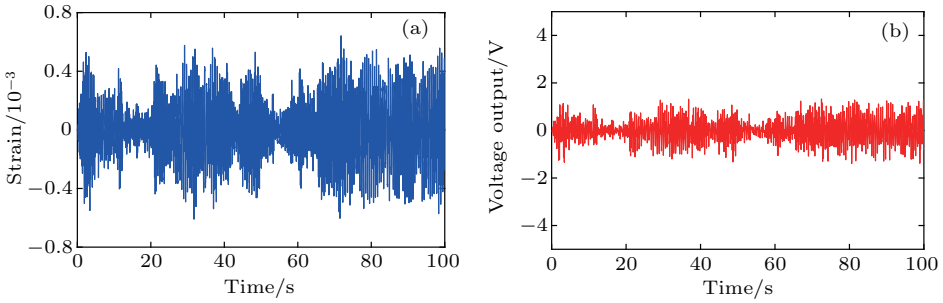


Fig. 18. Waveforms of strain and output voltage under the excitation of PSD = 0.15 m^2/s^3 (monostable system): (a) strain; (b) output voltage.

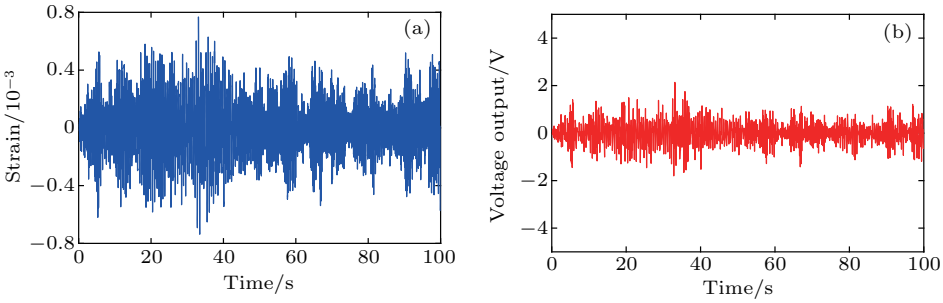


Fig. 19. Waveforms of strain and output voltage under the excitation of PSD = 0.2 m^2/s^3 (monostable system): (a) strain; (c) output voltage.

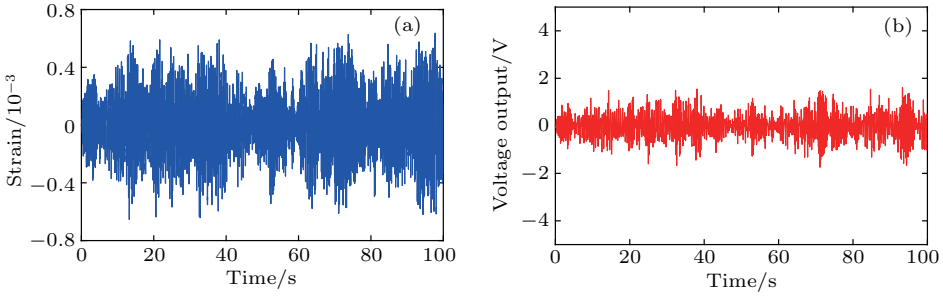


Fig. 20. Waveforms of strain and output voltage under the excitation of PSD = 0.25 m^2/s^3 (monostable system): (a) strain; (b) output voltage.

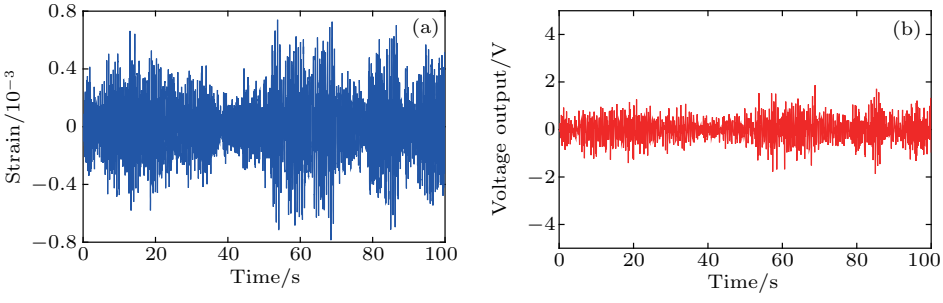


Fig. 21. Waveforms of strain and output voltage under the excitation of PSD = 0.3 m^2/s^3 (monostable system): (a) strain; (b) output voltage.

5.2. Buckling case

For the inverted beam, in the buckling state, considering its vertical displacement, the potential energy and restoring force can be given by

$$\begin{aligned} U &= \frac{1}{2}\mathrm{EIN}_2 q^2 + \frac{1}{2}\mathrm{EIN}_3 q^4 - \frac{1}{2}N_4\rho_\mathrm{b}A_\mathrm{b}gq^2 - \frac{1}{2}N_1 mgq^2, \\ &= -\frac{1}{2}\mathrm{EIN}_2\left(\frac{N_1 mg + N_4\rho_\mathrm{b}A_\mathrm{b}g}{\mathrm{EIN}_6} - 1\right)q^2 + \frac{1}{2}\mathrm{EIN}_3 q^4, \quad (22) \\ F &= -\mathrm{EIN}_2\left(\frac{N_1 mg + N_4\rho_\mathrm{b}A_\mathrm{b}g}{\mathrm{EIN}_2} - 1\right)q + 2\mathrm{EIN}_3 q^3, \quad (23) \end{aligned}$$

where

$$\begin{aligned} \kappa_1 &= -\mathrm{EIN}_2\left(\frac{N_1 mg + N_4\rho_\mathrm{b}A_\mathrm{b}g}{\mathrm{EIN}_2} - 1\right); \quad \kappa_2 = 2\mathrm{EIN}_3, \\ N_1 &= \int_0^{l_\mathrm{b}} (\psi')^2 \mathrm{d}y; \quad N_2 = \int_0^{l_\mathrm{b}} (\psi'')^2 \mathrm{d}y; \\ N_3 &= \int_0^{l_\mathrm{b}} (\psi'\psi'')^2 \mathrm{d}y; N_4 = \int_0^{l_\mathrm{b}} \left[\int_0^y (\psi')^2 \mathrm{d}\xi\right] \mathrm{d}y. \quad (24) \end{aligned}$$

The restoring force F indicates that the stiffness κ_1 varies with the mass of pendulum m. When $(N_1 mg + \rho_\mathrm{b}A_\mathrm{b}g)/\mathrm{EIN}_2 \leq 1$, the stiffness κ_1 is positive, the potential energy curve exhibits a single well and owns one equilibrium position, the system is monostable. With increasing pendulum mass m, $(N_1 mg + \rho_\mathrm{b}A_\mathrm{b}g)/\mathrm{EIN}_2 > 1$, the stiffness κ_1 becomes negative, and the corresponding potential energy owns double wells and two equilibrium positions. Thus, the original monostable system becomes a bi-stable one. This evolution is illustrated by the potential energy and restoring force curves as shown in Fig. 22.

For an inverted beam, the gravity of the pendulum mass will make it lose stability and begin buckling.[34–36] Increasing the weight of mass of the pendulum, the beam will begin to buckle at $m = 3$ g, which turns the system to a bi-stable one. To compare the system's performance in the bi-stable state, the excitation was designated as the same band-limited white noise as in the unbuckling case. The simulation results for the entity model in the COMSOL are shown in Figs. 23–28. First, at PSD $= 0.15$ m^2/s^3, the system oscillates around one of the two equilibrium positions, and the output voltage is very small (see Fig. 23); then the excitation increases to PSD $= 0.2$ m^2/s^3, the system begins to jump between the two equilibrium positions, and the corresponding output voltage increases accordingly (see Fig. 24); further increasing the excitation intensity to PSD $= 0.25$ m^2/s^3, the jumping times increase slightly, bringing about several spikes of voltage at those instants (see Fig. 25); increasing the excitation intensity to PSD $= 0.3$ m^2/s^3, it can be seen that there occurs a frequent jumping between the two equilibrium positions, leading to a large increase in output voltage (see Fig. 26); then at PSD $= 0.35$m^2/s^3 and PSD $= 0.4$ m^2/s^3, the jumping between two equilibrium positions becomes dense and there appear many spikes in the output voltage, with the maximum voltage nearly reaching 6 V (see Figs. 27 and 28). Thus, the results suggest that the bi-stable IPBP could achieve the larger output. We then give the curve of the tip displacement versus the stochastic excitation PSD, as plotted in Fig. 29(a). It is evident that the tip displacement will increase with increasing excitation intensity D.

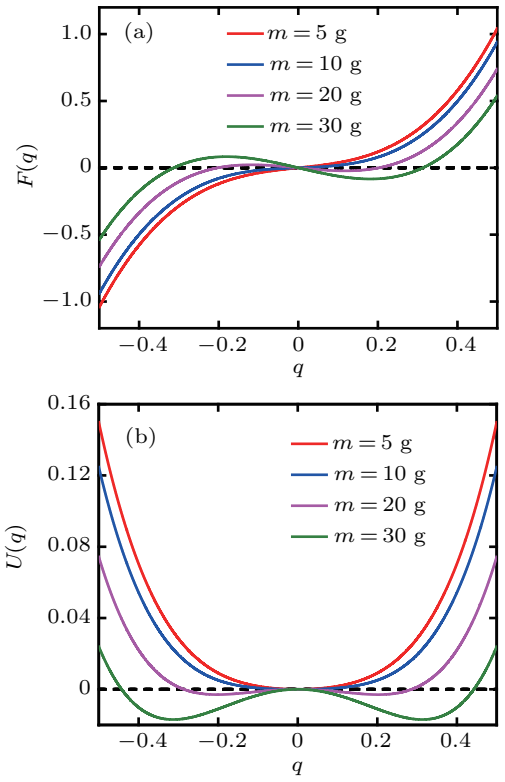


Fig. 22. Restoring force and potential energy.

To show the advantage of the proposed energy harvester, the average powers under stochastic excitation for the proposed bi-stable nonlinear system and the linear system are calculated. The linear system is composed of an inverted beam with a tip mass. The average power is defined as

$$P_\mathrm{ave} = \frac{1}{t_2 - t_1}\int_{t_2}^{t_1} \frac{V(t)^2}{R}\mathrm{d}t. \quad (25)$$

Figure 29(b) shows that the bi-stable nonlinear system could generate a much higher output compared to the linear one. Especially at $D = 0.4$ m^2/s^3, the average power of bi-stable system reaches 22.70 μW, while that of the linear system is only 0.65 μW.

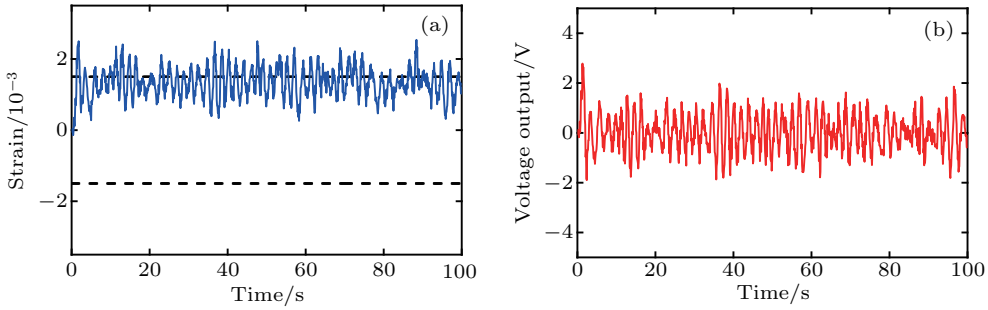


Fig. 23. Waveforms of strain and output voltage under the excitation of PSD = 0.15 m^2/s^3 (bi-stable system): (a) strain; (b) output voltage.

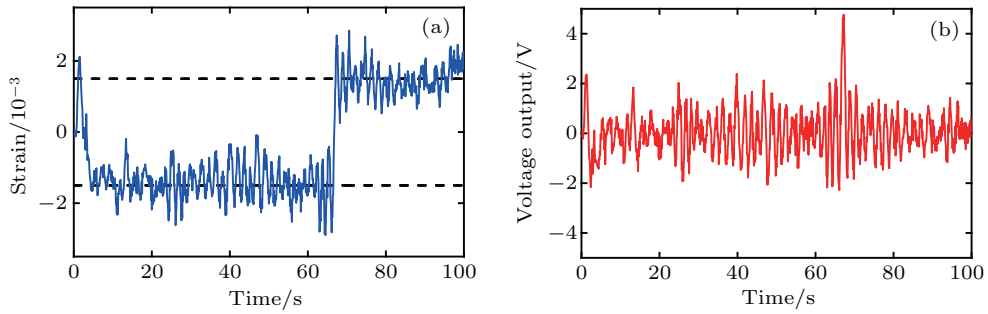


Fig. 24. Waveforms of strain and output voltage under the excitation of PSD = 0.2 m^2/s^3 (bi-stable system): (a) strain; (b) output voltage.

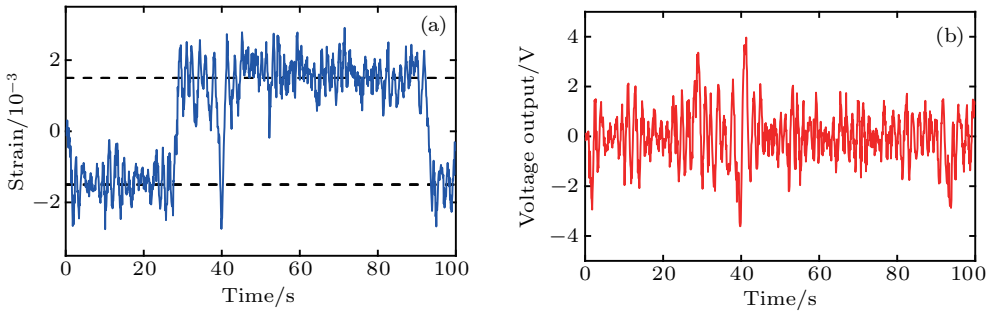


Fig. 25. Waveforms of strain and output voltage under the excitation of $D = 0.25$ m^2/s^3 (bi-stable system): (a) strain; (b) output voltage.

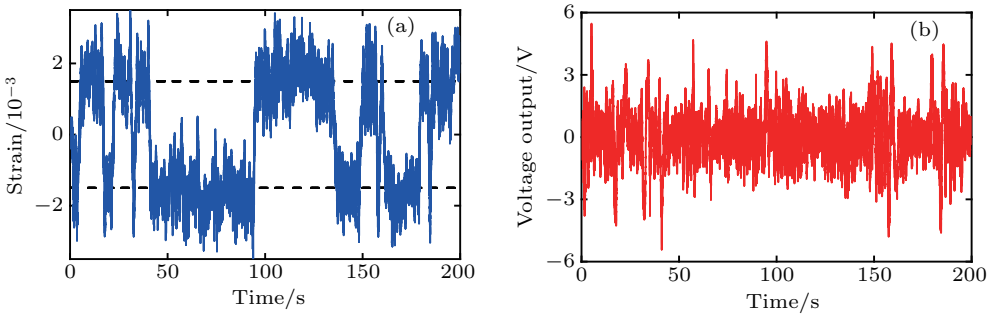


Fig. 26. Waveforms of strain and output voltage under the excitation of PSD = 0.3 m^2/s^3 (bi-stable system): (a) strain; (b) output voltage.

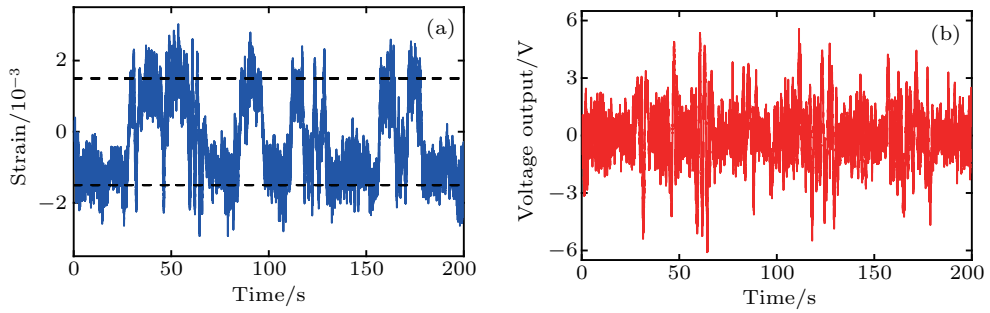


Fig. 27. Waveforms of strain and output voltage under the excitation of $D = 0.35$ m^2/s^3 (bi-stable system): (a) strain; (b) output voltage.

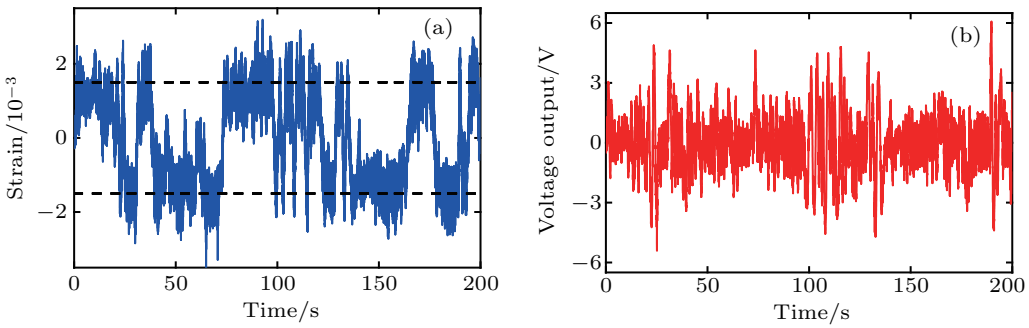


Fig. 28. Waveforms of strain and output voltage under the excitation of $D = 0.4\ \mathrm{m^2/s^3}$ (bi-stable system): (a) strain; (b) output voltage.

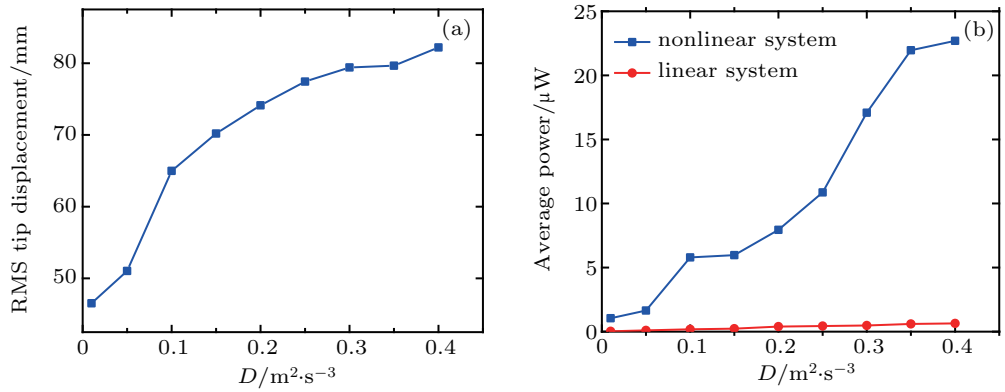


Fig. 29. Summarized rms tip displacement and average power at different excitation intensity D: (a) rms tip displacement; (b) average power.

6. Conclusions

In this study, a 2-DOF inverted piezoelectric beam with pendulum was proposed to harvest stochastic base excitation energy. It is proved that this configuration owns 1:3 super-harmonic resonance. The responses for sweeping frequency show that the system's nonlinearity bends the amplitude-frequency curves at the first and second natural frequency to different directions. With the variation of the pendulum mass, this configuration could be monostable or bi-stable. The results show that the bi-stable state outperforms the monostable state in harvesting stochastic energy when the excitation intensity is sufficient to induce the inter-well motion. In bi-stable state, the system can be excited to jump between the two equilibrium positions and give a large output. Especially under a relatively high excitation, the system can reach a dense jump between equilibrium positions and generate a considerably large output voltage. The combination of harmonic resonance and bi-stability could benefit a lot to the energy harvesting efficiency. In the future, more detailed studies including experiments will be performed for the IPBP.

Appendix A

By equating the coefficients associated with each harmonic term in Eqs. (19)–(21), we can get eighteen algebraic equations. Solving the algebraic equations, the unknown coefficients A_{ij} and B_{ij} $(i,j=1,2,3)$ in Eqs. (13)–(15) can be acquired. After balancing the first three harmonic terms, the eighteen algebraic coefficient equations can be obtained as follows:

$$-A_{11}\Omega^2 - r_m A_{21}\Omega^2 - r_m\left[\frac{1}{4}\Omega^2(A_{21}^3 + 5A_{21}^2A_{23} + A_{23}\left(8A_{22}^2 - 5B_{21}^2 - 8B_{22}^2\right) + 16A_{22}B_{22}B_{23}\right.$$
$$\left.+A_{21}(8A_{22}^2 + 18A_{23}^2 + B_{21}^2 + 8B_{22}^2 + 10B_{21}B_{23} + 18B_{23}^2))\right] + c_1'B_{11}\Omega + \hat{\omega}_1^2A_{11} + \chi'A_{31} + \frac{a_z}{l} = 0,$$
$$-B_{11}\Omega^2 - r_m B_{21}\Omega^2 - r_m\left[\frac{1}{4}\Omega^2(-10A_{21}A_{23}B_{21} + 18A_{23}^2B_{21} + B_{21}^3 + 16A_{22}A_{23}B_{22} + 8B_{21}B_{22}^2 + 8A_{22}^2\left(B_{21} - B_{23}\right)\right.$$
$$\left.-5B_{21}^2B_{23} + 8B_{22}^2B_{23} + 18B_{21}B_{23}^2 + A_{21}^2\left(B_{21} + 5B_{23}\right))\right] - c_1'A_{11}\Omega + \hat{\omega}_1^2B_{11} + \chi'B_{31} = 0,$$
$$-4A_{12}\Omega^2 - 4r_m A_{22}\Omega^2 - r_m\left[\frac{1}{2}\Omega^2(A_{21}^2A_{22} + 2A_{22}^3 + 5A_{23}B_{21}B_{22} + 5A_{21}\left(A_{22}A_{23} + B_{22}B_{23}\right)\right.$$

$$+A_{22}\left(9A_{23}^2+B_{21}^2+2B_{22}^2-5B_{21}B_{23}+9B_{23}^2\right)\Big)\Big]+2c_1'B_{12}\Omega+\hat{\omega}_1^2A_{12}+\chi'A_{32}=0,$$

$$-4B_{12}\Omega^2-4r_mB_{22}\Omega^2-r_m\Big[\frac{1}{2}\Omega^2(2A_{22}^2B_{22}+5A_{22}\left(A_{23}B_{21}+A_{21}B_{23}\right)$$

$$+B_{22}(A_{21}^2-5A_{21}A_{23}+9A_{23}^2+B_{21}^2+2B_{22}^2+5B_{21}B_{23}+9B_{23}^2))\Big]-2c_1'A_{12}\Omega+\hat{\omega}_1^2B_{12}+\chi'B_{32}=0,$$

$$-9A_{13}\Omega^2-9r_mA_{23}\Omega^2-r_m\Big[-\frac{1}{4}\Omega^2(A_{21}^3-2A_{21}^2A_{23}-3A_{21}B_{21}^2$$

$$-A_{23}(8A_{22}^2+9A_{23}^2+2B_{21}^2+8B_{22}^2+9B_{23}^2))\Big]+3c_1'B_{13}\Omega+\hat{\omega}_1^2A_{13}+\chi'A_{33}=0,$$

$$-9B_{13}\Omega^2-9r_mB_{23}\Omega^2-r_m\Big[\frac{1}{4}\Omega^2(B_{21}^3+\left(8A_{22}^2+9A_{23}^2+2B_{21}^2+8B_{22}^2\right)B_{23}$$

$$+9B_{23}^3+A_{21}^2\left(-3B_{21}+2B_{23}\right))\Big]-3c_1'A_{13}\Omega+\hat{\omega}_1^2B_{13}+\chi'B_{33}=0,$$

$$-A_{21}\Omega^2-A_{11}\Omega^2+c_2'B_{21}\Omega+\hat{\omega}_2^2A_{21}+\frac{a_z}{l}=0,\quad -B_{21}\Omega^2-B_{11}\Omega^2-c_2'A_{21}\Omega+\hat{\omega}_2^2B_{21}=0,$$

$$-4A_{12}\Omega^2-4A_{22}\Omega^2+2c_2'B_{22}\Omega+\hat{\omega}_2^2A_{22}=0,\quad -4B_{12}\Omega^2-4B_{22}\Omega^2-2c_2'A_{22}\Omega+\hat{\omega}_2^2B_{22}=0,$$

$$-9A_{23}\Omega^2-9A_{13}\Omega^2+3c_2'B_{23}\Omega+\hat{\omega}_2^2A_{23}=0,\quad -9B_{23}\Omega^2-9B_{13}\Omega^2-3c_2'A_{23}\Omega+\hat{\omega}_2^2B_{23}=0,$$

$$\frac{A_{31}}{R}-\chi B_{11}\Omega+C_pB_{31}\Omega=0,\quad \frac{B_{31}}{R}+\chi A_{11}\Omega-C_pA_{31}\Omega=0,$$

$$\frac{A_{32}}{R}-2\chi B_{12}\Omega+2C_pB_{32}\Omega=0,\quad \frac{B_{32}}{R}+2\chi A_{12}\Omega-2C_pA_{32}\Omega=0,$$

$$\frac{A_{33}}{R}-3\chi B_{13}\Omega+3C_pB_{33}\Omega=0,\quad \frac{B_{33}}{R}+3\chi A_{13}\Omega-3C_pA_{33}\Omega=0.$$

References

[1] Anton S R and Sodano H A 2007 *Smart Mater. & Struct.* **16** R1
[2] Daqaq M F, Masana R, Erturk A and Quinn D D 2014 *Appl. Mech. Rev.* **66** 040801
[3] Harne R L and Wang K W 2013 *Smart Mater. Struct.* **22** 023001
[4] Stanton S C, McGehee C C and Mann B P 2010 *Physica D* **239** 640
[5] Tao K, Tang L H, Wu J, Lye S W, Chang H L and Miao J M 2018 *J. Microelectromech. Syst.* **27** 276
[6] Ferrari M, Ferrari V, Guizzetti M, Ando B, Baglio S and Trigona C 2010 *Sens. Actuator A-Phys.* **162** 425
[7] Ferrari M, Bau M, Guizzetti M and Ferrari V 2011 *Sens. Actuator A-Phys.* **172** 287
[8] Leadenham S and Erturk A 2014 *J. Sound Vibr.* **333** 6209
[9] Kang-Qi, Chun-Hui, Wang, Wei-Dong, Fang and Yang 2014 *Chin. Phys. B* **23** 084501
[10] Chen L Q and Jiang W A 2015 *J. Appl. Mech.-Trans. ASME* **82** 031004
[11] Chen L Q, Jiang W A, Panyam M and Daqaq M F 2016 *J. Vib. Acoust.-Trans. ASME* **138** 061007
[12] Jiang W A, Chen L Q and Ding H 2016 *Nonlinear Dyn.* **85** 2507
[13] Yang W and Towfighian S 2017 *Smart Mater. Struct.* **26** 095008
[14] Xu J W and Tang J O 2017 *J. Intell. Mater. Syst. Struct.* **28** 323
[15] Xu J and Tang J 2015 *Appl. Phys. Lett.* **107** 213902
[16] Xiong L Y, Tang L H and Mace B 2018 *Nonlinear Dyn.* **91** 1817
[17] Xiong L, Tang L and Mace B R 2016 *Appl. Phys. Lett.* **108** 203901
[18] Wu Y P, Ji H L, Qiu J H and Han L 2017 *Sens. Actuator A-Phys.* **264** 1
[19] Gao Y J, Leng Y G, Fan S B and Lai Z H 2014 *Acta Phys. Sin.* **63** 090501 (in Chinese)
[20] Li H T and Qin W Y 2016 *Chin. Phys. B* **25** 110503
[21] Zhang Y Y, Leng Y G, Tan D, Liu J J and Fan S B 2017 *Acta Phys. Sin.* **66** 220502 (in Chinese)
[22] Erturk A, Hoffmann J and Inman D J 2009 *Appl. Phys. Lett.* **94** 254102
[23] Zhou S X, Cao J Y, Erturk A and Lin J 2013 *Appl. Phys. Lett.* **102** 173901
[24] Li H T, Qin W Y, Lan C B, Deng W Z and Zhou Z Y 2016 *Smart Mater. Struct.* **25** 015001
[25] Zhou S X and Zuo L 2018 *Commun. Nonlinear Sci. Numer. Simul.* **61** 271
[26] Lan C and Qin W 2017 *Mech. Syst. & Signal Process.* **85** 71
[27] Bilgen O, Friswell M I, Ali S F and Litak G 2015 *Int. J. Struct. Stab. Dyn.* **15** 1450038
[28] Friswell M I, Ali S F, Bilgen O, Adhikari S, Lees A and Litak G 2012 *J. Intell. Mater. Syst. Struct.* **23** 1505
[29] Borowiec M, Litak G, Friswell M I and Adhikari S 2014 *Int. J. Structural Stability & Dyn.* **14** 1440018
[30] Masuda A, Senda A, Sanada T and Sone A 2013 *J. Intell. Mater. Syst. Struct.* **24** 1598
[31] Sebald G, Kuwano H, Guyomar D and Ducharne B 2011 *Smart Materials & Structures* **20** 102001
[32] Su D X, Nakano K, Zheng R C and Cartmell M P 2015 *Proc. Inst. Mech. Eng. Part. C-J. Eng. Mech. Eng. Sci.* **229** 3308
[33] Westermann H, Neubauer M, Wallaschek J and Asme 2012 *Proceedings of the Asme Conference on Smart Materials, Adaptive Structures and Intelligent Systems*, Vol. 2 pp. 803–810
[34] Ando B, Baglio S, Bulsara A R and Marletta V 2014 *Sens. Actuator A-Phys.* **211** 153
[35] Eltanany A M, Yoshimura T, Fujimura N, Ebied M R and Ali M G S 2017 *Jpn. J. Appl. Phys.* **56** 10pd02
[36] Xu C D, Liang Z, Ren B, Di W N, Luo H S, Wang D, Wang K L and Chen Z F 2013 *J. Appl. Phys.* **114** 114507